Water and Soil Management and Modeling

Online ISSN: 2783 - 2546

University of Mohaghegh Ardabili

Indirect estimation of Arvand River discharge using numerical modeling and remote sensing: A novel approach in water resources management

Abbas Einali[1*], Masoud Sadrinasab[2], Mohammad Akbarinasab[3], Jafar Azizpour[4]

[1] Assistant Professor of Physical Oceanography, Faculty of Environmental and Marine Sciences, University of Mazandaran, Mazandaran, Iran
[2] Associate Professor of Physical Oceanography, Department of Environmental Design, University of Tehran, Tehran, Iran
[3] Associate Professor of Physical Oceanography, Faculty of Environmental and Marine Sciences, University of Mazandaran, Mazandaran, Iran
[4] Assistant Professor of Physical Oceanography, Iranian National Institute for Oceanography and Atmospheric Science, Tehran, Iran

Abstract
The river discharge is the most critical parameter in the hydrologic cycle, and its measurement is vital considering climate change and water resource management. Due to local problems, the discharge of the Arvand River, located in the Middle East (hot-dry climate), has not yet been measured directly. The Arvand River is considered the main source of freshwater inflow in the Persian Gulf and plays an essential environmental role in the northwest coastal zones of the Persian Gulf. For this reason, an indirect method was derived and used for the Arvand River discharge in this study. This method estimates the river discharge based on the river plume dimension. For this purpose, numerical modeling extracted the relationship between river discharge and river plume area in the first part. Thus, the Persian Gulf's temperature, salinity, and water circulation were modeled using FVCOM. In the following, the sensitivity of the river plume to the discharge and wind was investigated more accurately by applying fourteen different wind modes plus eight different discharge modes to the model. The numerical model results indicate that the river plume of Arvand is a "surface-advected plume" with a high sensitivity to wind fluctuations. Numerous experiments extracted the mathematical relation between the Plume Area and the River Discharge (PA-RD) within various wind conditions. A surface salinity of 37 psu determined the river plume border. The second step extracted the Arvand River plume (salinity plume) area using remote sensing techniques. The linear relationship between the sea surface salinity in situ measurements and surface reflectance (SSS-SR) of Landsat TM5 satellite bands was obtained using a regression model at the river mouth in 1992. The surface salinity pattern at the Arvand River mouth was revealed by applying the SSS-SR relation to all of the Landsat pixels. Eventually, in 1992, the river plum (salinity plume) area was extracted, and then by substituting it in the PA-RD relation, the river discharge was estimated at 540 $m^3.s^{-1}$. The present work is the first serious step toward studying the Arvand River discharge.
Keywords: River Discharge, FVCOM, Landsat TM5, Arvand River, River Plume, Sea Surface Salinity

Article Type: Research Article

*Corresponding Author, E-mail: a.einali84@umz.ac.ir
Citation: Einali, A., Sadrinasab, M., Akbarinasab, M., & Azizpour, J. (2025). Indirect estimation of Arvand River discharge using numerical modeling and remote sensing: A novel approach in water resources management, Water and Soil Management and Modeling, 5(4), 277-300.
doi: 10.22098/mmws.2025.18232.1662
Received: 01 September 2025, Received in revised form: 10 October 2025, Accepted: 25 October 2025, Published online: 07 November 2025
Water and Soil Management and Modeling, Year 2025, Vol. 5, No. 4, pp. 277-300.
Publisher: University of Mohaghegh Ardabili

1. Introduction

River discharge is a significant measurable variable that is vital due to climate change and the water crisis, especially for dry, hot, and desert areas (Duvvuri et al., 2024; Eddin et al., 2025), such as the Arvand River region. Unfortunately, until now, the Arvand River discharge has not been measured, so there is no data on the river discharge and its changes (Global Runoff Data Centre (GRDC)). However, there are signs of warming and drought in the river catchment area. The average temperature has increased over the last years, while average precipitation has decreased to the long-term average (Duenwald et al., 2022; Karami, 2019). Furthermore, water harnessing and dam building on upstream sources decreased the Arvand River discharge (Al-Aesawi et al., 2021).

1.1. River discharge measurement

Water rivers discharged into the coasts indicate the essential relationship between the sea and land systems (Gonçalves et al., 2012). River discharge measurement is necessary for water source management, power generation, floodwater forecast and control, and understanding local and global hydrologic cycles. A river's discharge specification (quality and rate) at its mouth is a general and immediate indicator of events in the watershed. So, continuous river discharge measurement, even daily, is vital in river research. There have been many efforts to improve international accessibility to information on water resources, but many countries do not share this information, and our knowledge is incomplete. On the other hand, many rivers form international borders and cross several countries. Upstream countries want to use more water resources and, for this reason, restrict river information sharing, especially river discharge. The water-conflict scenario cannot be dismissed (Robert Brakenridge et al., 2012). Therefore, measuring and sharing rivers' discharge is necessary for oceanography, coastal engineering, and biology.

There are various ways to measure river discharge, which are divided into two methods: direct and indirect. In the direct method, in situ measurements on an intended river transect are necessary. Many rivers are located in inaccessible and remote places, so their river discharge measurement is impossible by direct methods. River discharge measurement for some others is impractical due to political and security problems. Despite accessibility, the Arvand River discharge has not been measured until now because the river is a political border between Iran and Iraq, and is related to issues. Therefore, indirect methods are best for measuring the Arvand River discharge. Emerging non-contact methods for discharge estimation, such as analyzing hydraulic patterns from imagery (Legleiter et al., 2025), demonstrate a growing shift toward image-based and indirect approaches. This tendency underscores the increasing importance of remotely observable indicators in rivers where direct measurements remain constrained. In the indirect method, the river discharge is estimated by extracting the relationship between river discharge and one of the visual characteristics of the river. These methods are low-cost, accessible, practical, and available anywhere. The Hydro-21 committee explicitly introduces remote sensing and indirect methods as the best and most common ways for river discharge measurement in the future (Cheng, 2000).

The visual characteristic of river plumes is one parameter used in indirect methods for river discharge measurement. River discharge is estimable using the relation between river discharge and river plume dimension. Osadchiev (2015) has investigated the plume of the Sochi and Mzymta rivers on the east coast of the Black Sea to quantify river discharge using numerical modeling and remote sensing. The study developed an approach for estimating river discharge by utilizing satellite images and numerical modeling based on converting visual characteristics of a river plume, detectable by remote sensing, to river discharge. This method has the advantage of detecting the plumes of small rivers, which are not always detectable by all satellites. Additionally, it can continuously measure the discharge of small rivers. They estimate river discharge using a combination of remote sensing and numerical modeling. The process involves modeling the river plume and its dimensions, concurrently detecting its dimensions through remote sensing, and using mathematical equations (river discharge – river plume dimensions equation) to estimate the river discharge. The study revealed that the estimated river discharge using the indirect method matched the measured river discharge obtained through the direct method, with an absolute error of 15% and a coefficient of determination (R^2) of 95% for this method (Osadchiev, 2015).

Gonçalves et al. (2012) researched the Douro River plume northwest of Portugal. The study involved extracting the river plume area using remote sensing and investigating its correlation with river discharge. The TSM factor was utilized to detect the river plume border. Satellite images were employed to calculate the river plume area corresponding to the river discharge. The river discharge is obtained from the measuring station located at an upstream dam. An excellent correlation of 0.719 was observed between the river plume area and river discharge, which reached 0.838 in some cases. Generally, the specified relationship between river discharge and plume area is used for river discharge estimation (Gonçalves et al., 2012).

In another study on the Karun River, as one of the tributaries of the Arvand River, an indirect method for river discharge measurement was employed. In that study, which was done by Tayfehrostami et al. (2021), changes in water level were also used as a parameter for indirect river discharge estimation. They utilized Sentinel-3B altimetry data and Sentinel-1 and Sentinel-2 imagery to extract water level and river width, correlating them to discharge via regression. This approach, akin to ours, relies on a visual characteristic of the river and demonstrates that remote sensing serves as an effective tool for discharge monitoring in areas with limited in-situ data (Tayfehrostami et al., 2021).

1.2. River plume

The river plume is a crucial phenomenon in coastal zones. In zones where the river discharge is significant, the plume influences the coastal dynamics and river-borns, including sediment, nutrients, and contaminants (Garvine, 1995). The nature of the river plume is variable (Gonçalves et al., 2012). The river plume may have different structures depending on the coastal streams, floor Bathymetry, and the characteristics of the inlet water (Yankovsky & Chapman, 1997).

The structure of the river plume is classified into two categories. First, the front between the coastal waters and the plume extends from the surface to the bottom. This type of plume is known as a "bottom-advected plume"; in this type, the density front (plume boundary) extends from the surface to the bottom. Second, the low-density river freshwater is located in the coastal waters. In this type of plume, called a "surface-advected plume", the river freshwater may extend up to a great distance from the beach and, except in the very close zones with the beach, has little or no direct interaction with the seafloor. Indeed, the plumes may also exhibit a mode between the two types, where the buoyancy flux interacts with the seafloor up to a certain distance before expanding towards the sea. Although these two plume types are similar in some cases, such as the density differences between the plume and the coastal streams and the effects caused by the Coriolis force, they have many differences concerning spatial scales and the characteristics of their flux and dynamics. The surface-advected plume's structure and motion depend on factors other than river discharge, such as wind and tidal currents (Yankovsky & Chapman, 1997).

In recent decades, the importance of the river plume perception has led many scientists to investigate the plume dynamics using mathematical models. Chao and Boicourt (1986) were the first to examine the structure of a plume and the streams created by it in parallel with the coast through numerical modeling (Chao & Boicourt, 1986). Xing and Davies (1999) demonstrated that wind shear stress increases vertical mixing and, therefore, affects the vertical and horizontal structure of the plume (Xing & Davies, 1999). Garvine (1981) and Garvine (1982) studied the Coriolis Effect on the plume, while Wiseman and Garvine (1995) examined the effects of coastal morphology on the plume. (Chao, 1988); Kourafalou et al. (1996) raised the significance of the tide in 1988 and 1996, respectively. The study indicated that the tide causes the plume to mix more vertically and expand horizontally at a slower rate (Καμίδης et al., 2015).

In a study by Kamidis et al. (2015), external forces influencing the formation velocity, size, and shape of the Nestos River plume were investigated. The results indicated that the tide has no specific effect on the plume dimensions far from the beach (Καμίδης et al., 2015). In other words, including studies conducted by Liu et al. (1999) and Bricker et al. (2006), similar results were reported in investigating the effect of the tide on the river plume (Bricker et al., 2006; Liu et al., 1999).

1.3. Sea surface salinity remote sensing

The techniques for remotely sensing water surface salinity are divided into two: direct and indirect methods. The physical basis of the seawater surface salinity direct sensing (both by satellite and by airplane) is shortwave brightness Temperature (bT). The bT is proportional to the water salinity. Several researchers, including Klein and Swift (1977), Swift and Mcintosh (1983), and Lagerloef et al. (1995), have provided comprehensive discussions in this regard (Koblinsky et al., 2003). The study of Chesapeake Bay using the airplane system by Miller is an example of successful research in this field that has been conducted in recent years (Miller et al., 1998). In the indirect measurement technique of water surface salinity using satellite imagery, the concentration of Colored Dissolved Organic Matter (CDOM) plays a vital role. Since CDOM is an intermediate operator between the reflexivity measured by satellite and surface salinity, the empirical relationship between CDOM and salinity is considered essential. In relation, it is assumed that the fresh and CDOM-free river water is conservatively mixed with seawater with a concentration of CDOM; as a result, there is a relationship between CDOM and salinity. Since CDOM can be measured remotely, we can calculate the degree of salinity from remote sensing observations. It is worth mentioning that this technique is only applicable in systems where the mixing of river water and coastal waters is done conservatively. Since surface salinity is a function of CDOM concentration, it is also a function of light reflexivity, an essential parameter in remote sensing. However, this assumption can be assured that the surface salinity is directly proportional to the reflection of the coloured bands of the satellite from the ocean surface (Urquhart et al., 2012).

The Landsat satellite is one of the most well-known Earth-observing satellites used to study and monitor the coastal zones. Free satellite imagery, good Spatial Resolution (SR), good Temporal Resolution (TR), and, most importantly, providing images containing scientific and continuous information about the water cycle, climate, ecosystem, and earth changes for about 40 years are among the main reasons for the selection of this satellite by most researchers. Landsat also provides the researchers with calibrated information with radiometric corrections. In light of the mentioned advantages, scientists have used Landsat images to estimate the salinity of the rivers, firths, gulfs, and coastal waters for decades (Selch, 2012). The use of satellite-derived sea surface salinity (SSS) for monitoring river plumes has recently achieved notable success (Ma et al., 2025). This trend indicates that employing indirect indicators to explore the relationship between discharge and plume characteristics is increasingly emphasized in recent studies.

Different experimental models have been used to estimate the seawater surface salinity from Landsat images. In most of these models, the relationship between in-situ salinity data and the satellite image bands data is determined using regression techniques (Selch, 2012). Khorram (1982) conducted the first study to indirectly measure the seawater surface salinity in San Francisco Bay. This study collected the Digital Numbers (DN) of the Landsat Multispectral Scanner System (MSS) sensor and surface salinity measurements data in September 1987. This study was the first attempt to successfully use the DNs of the Landsat satellite imagery to produce a salinity map using Digital Image Processing (DIP) in this zone (Khorram, 1982). Selch (2012) compared the models of estimating seawater surface salinity using the remote sensing technique in Whitewater Bay. In this study, in situ measurements of the water surface salinity with Landsat TM 5 were examined in a cross-referenced analysis. DNs of each satellite image were extracted in areas with in-situ surface salinity data. Water salinity and satellite imagery bands were considered dependent and explanatory variables. The geographically weighted regression (GWR) performed better than other regression models (Selch, 2012).

The Persian Gulf is a semi-closed shallow basin with the largest source of crude oil and gas, and it is connected to the Gulf of Oman in the east and to the northwest zones of the Indian Ocean through the Strait of Hormuz (Jafar et al., 2014). The Arvand River is the primary freshwater source in the Persian Gulf and plays an essential ecological role in the northwest coastal zones. The Arvand River is formed by the confluence of the Euphrates (Iraq), the Tigris (Iraq and Turkey), Karun, and Karkheh (Iran) rivers. The watershed of the Arvand River, with more than 900,000 km^2, is the settlement for about 54 million people in Iran, Iraq, Syria, and Turkey. The mouth of the river is about 700 m in width (UN-ESCWA, 2013).

By this time, different evaluations have been conducted on the Arvand River discharge. Two points are worth mentioning. First, these assessments have never been obtained from accurate and continuous measurements. Second, now, the discharge of this river is indeterminate due to the lack of in-situ measurement data (especially after the construction of upstream dams, which have resulted in a severe decrease in the river discharge) (Kämpf & Sadrinasab, 2006). Oceanographic studies are infeasible in the river and its mouth due to the region's governing geographical, political, and security conditions, so its discharge has not yet been measured. Therefore, we inevitably used the river plume characteristics to obtain river discharge information. The current study is the first serious step in investigating the Arvand River discharge. This study estimated the Arvand River discharge using a suggested indirect method. The river plume dimension and its relationship to river discharge are the basis of this indirect method. Hence, the method of this paper is divided into two parts: 1-numerical modeling (for the extraction relationship between river discharge and salinity river plume area) and 2- Remote sensing (detection of salinity river plume). Accordingly, the area of the Arvand River plume in March 1992 was extracted using satellite imagery, and the river discharge was estimated using the extracted relationship between river discharge and its plume. The reason for choosing this date to perform this method was the availability of appropriate satellite imagery and field data.

2. Materials and Methods

The methods used in this study fall into two parts. In one part, the Arvand River plume was simulated using numerical modeling, and its sensitivity to river discharge and wind was investigated. The criterion for measuring the river plume area is based on the surface salinity. This section obtained the relationship between the plume area and the river discharge (PA-RD) under different wind conditions. It should be noted that the impossibility of in-situ measurement has promoted the performance of numerical modeling for studying the river plume. In the other part, the surface salinity and the plume area were determined using the results of the Landsat satellite imagery from 1992. Finally, the river discharge was estimated that year by substituting the plume area (yield from the satellite images processing) in the PA-RD relation. The methods are described in detail below.

2.1. hydrodynamic simulation

In the present study, a 3D Finite Volume Community Ocean Model (FVCOM) has been applied, which has an unstructured grid, free-surface, and the governing equations of ocean circulation. Unlike the finite element and finite difference methods that benefit from the differential form of governing equations, in this model, the integral form of governing equations has been applied. In the computational field, the finite volume technique would better satisfy the conservation of mass condition since integral equations are numerically solved by flux calculations over a triangular mesh of an arbitrary size (like the finite element method). From a technical and specialized point of view, FVCOM includes the properties of finite-difference (concerning the simplicity of discretization of codes and computational usefulness) and finite-element (a suitable geometry of the environment) methods. The basic equations of the model include momentum, continuity, temperature, salinity, and density equations (Chen et al., 2006).

To pick out Horizontal Diffusion Coefficients in the FVCOM, the user can use constant values or the Smagorinsky model (Smagorinsky, 1963). One of the most prominent features of FVCOM is the application of an up-to-date version of the Oceanic Turbulence MY-2.5 model for the parameterization of the vertical eddy viscosity coefficient and vertical thermal diffusion (Mellor & Yamada, 1982).

The FVCOM simulation domain encompassed the entire Persian Gulf basin and part of the Oman Sea, covering the geographical range of 22.53°–30.49°N and 47.78°–59.81°E (Figure 1). This spatial coverage was selected to ensure that the hydrodynamic exchanges between the Persian Gulf and the Oman Sea were properly represented. At the eastern open boundary (approximately 59.81°E), open boundary conditions were imposed to allow the inflow and outflow of water with the Oman Sea, whereas the remaining boundaries were defined as closed or coastal. This configuration enabled tidal forcing and sea-level variability from the Oman Sea to be naturally introduced into the model and to influence the dynamics of the Arvand River plume. At this open boundary, tidal forcing was prescribed based on the Admiralty Tide Tables. In addition, wind forcing and hydrographic conditions (temperature and salinity) were imposed according to available datasets to initialize and drive the model simulations.

Bathymetric data for the whole computational domain were primarily obtained from the GEBCO_08 global dataset with a spatial resolution of 30 arc-seconds (IOC, 2003). To improve accuracy in the near-field region, particularly at the Arvand River mouth, local bathymetric data with a spatial resolution of 30 m were incorporated. The combination of global and high-resolution local data provided a more accurate representation of the bottom topography near the river mouth and reduced potential errors associated with excessive smoothing in the global dataset (Figure 2).

The specialized SMS 10.1, 2010 software produced a computational domain with variable spatial resolution. The computational mesh was generated as an unstructured triangular grid, consisting of 12,243 nodes and 19,332 elements. The grid spacing varied from about 250 m near the Arvand River mouth to approximately 32 km at the open boundary (Figure 2). To examine numerical stability and accuracy, a mesh convergence test was performed using three grids of varying resolution (coarse, medium, and fine). The comparison of diagnostic variables showed that the relative difference between the medium and fine grids in terms of surface salinity distribution was less than 5%, and the difference in tidal amplitude at the validation station was below 3%. These results demonstrate that the selected medium-resolution mesh provides numerically converged solutions and is sufficient for analyzing the Arvand River plume dynamics.

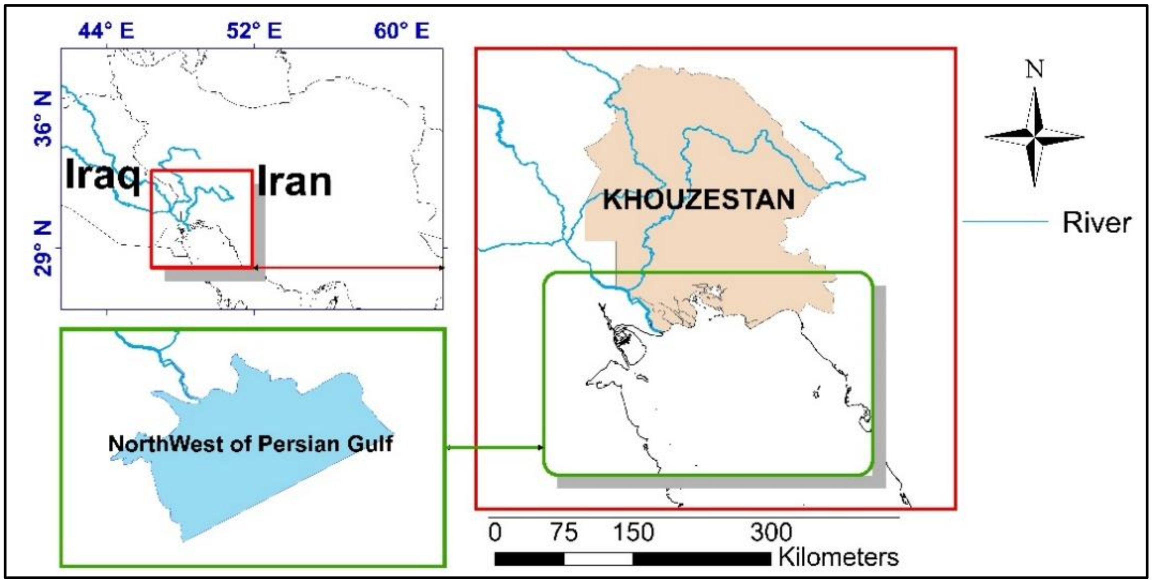

Figure 1. Location of the Arvand River and its watershed in Iran (Khuzestan province) and Iraq, and study area: northwest of the Persian Gulf

The time steps of the internal and external modes of the model were 3 and 10 s, respectively. The time step of the external mode has been achieved by the Courant Friedrich Levy (CFL) stability condition (Chen et al., 2006). The water surface fluctuations in the open boundary points have been applied as amplitudes and phases, which cover the tidal constituents, including M_2, S_2, K_1, and O_1, that cover more than 90% of tidal energy. The information is derived from the Tidal Model Driver (TMD) model. Wind, rain, evaporation, and heat flux data were obtained from the European Center for Medium-Range Weather Forecasts (ECMWF) database, with a temporal resolution of 6 hours and a spatial resolution of 0.25 degrees (approximately 28 km). The wind data were specifically extracted at a height of 10 meters above the surface. To integrate these data into the FVCOM computational grid, bilinear interpolation was applied to spatially align the ECMWF data with the model's unstructured triangular grid, followed by inverse distance-weighted averaging to ensure smooth temporal and spatial transitions across the domain. Indeed, the meteorological data used in this modeling phase varies regarding place and time. The Hybrid Coordinate Ocean Model (HYCOM) output was used for time series temperature and salinity profiles at the open boundary nodes. The freshwater inlet to the model is the confluence of the Arvand and Karun Rivers, the beginning of the Arvand River (Figure 2). As mentioned before, no proper assessment of the Arvand River discharge has been conducted up until now. According to Kämpf and Sadrinasab (2006), the Arvand River discharge is considered to be about 300-650 $m^3.s^{-1}$, which changes sinusoidally throughout the year (the minimum and maximum discharges with an annual average of 500 $m^3.s^{-1}$ belong to October and April, respectively). Based on the measurements, the water salinity in the freshwater inlet is considered 2 ppt. According to (Kämpf & Sadrinasab, 2006), the river water temperature of the model was set to 16 to 32°C. Additionally, the model was run with initial conditions for surface temperature and water level fluctuations. The model has been executed in the baroclinic mode and within 20 layers. One of the apparent features of the FVCOM is the layers' unequal distance adjustment. In this model, the thickness of the surface layer is less than that of the deep layers. The model's vertical and horizontal mixing used the MY2.5 and Smagorinsky methods, respectively. The model was executed for 5 years, and the last year's results were selected as modeling results. It is also necessary to explain that, given that the ultimate goal of this study is to estimate the river discharge in March when there is a suitable satellite image and relevant measurement data of sea surface salinity at the river mouth, the model results in this month were used to conduct simulations related to the relationship between river discharge and plume area.

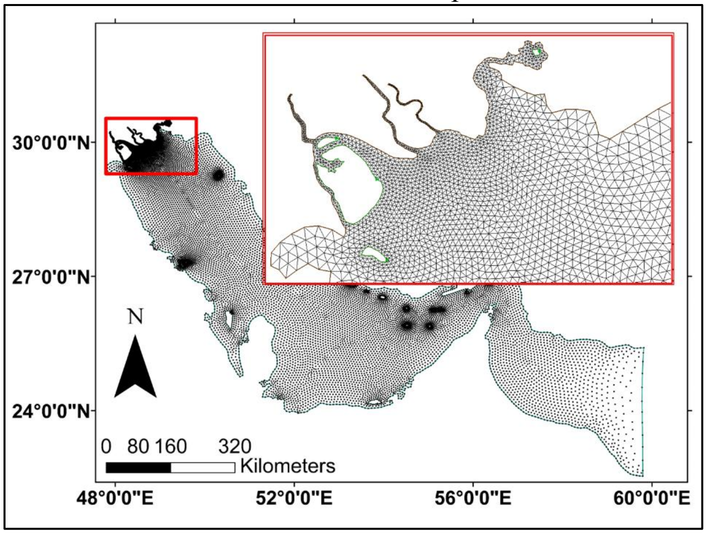

Figure 2. Model computational domain in the north-western part of the Persian Gulf and the freshwater inlet to the Persian Gulf.

After executing the model for the whole zone, the influences of the river discharge and wind on the structure of the river plume were examined by conducting experiments at the river mouth. To examine the impact of wind on the river's plume, 14 different wind scenarios were selected to encompass the range of wind patterns present in the region. To this end, the results of a study conducted by KOMIJANE et al. (2014) were used. The 14 wind modes are north, south, west, and east winds of 2 and 4 $m.s^{-1}$, northwest and southeast winds of 8 $m.s^{-1}$, northwest and southeast winds of 14 $m.s^{-1,}$ and windless conditions.

In order to study the effects of the river discharge fluctuations, eight different modes were considered for each wind mode. Based on the (Kämpf & Sadrinasab, 2006) study, the selected discharges were set to 300, 350,400, 50, 500, 550, 600, and 650 $m^3.s^{-1}$. Therefore, 112 different modes were implemented for the discharge-wind conditions.

2.2. Remote sensing

Several empirical models have been applied to measure surface salinity using Landsat data. In these models, the relationship between the measured salinity data and the bands for satellite image data is determined using the regression methods (Selch, 2012). The best oceanographic dataset with an appropriate spatial range and the closest gauging stations to the Arvand River mouth was obtained from the Regional Organization for the Protection of the Marine Environment (ROPME) oceanographic cruises in 1992. Concerning these descriptions and all the benefits of the Landsat sensor, its application is inevitable. This study utilized surface salinity data obtained during the ROPME oceanographic cruises in April 1992. These measurements, characterized by extensive spatial coverage and standardized observational protocols, represent the most reliable source for capturing regional surface conditions. For the remote sensing part, the Landsat TM-5 image closest in acquisition date to the field measurements was selected, taking into account adequate spatial coverage and constraints such as cloud presence. We use regression and correlation to study the relationship between the two variables. The correlation indicates how close the relationship between two variables is to a straight line. The regression predicts the independent variable's values from the dependent variable's by forming an equation (Townend, 2013). In the present work, the correlation coefficient means Pearson's product-moment correlation coefficient, and the regression means simple linear regression. The surface reflectance of different bands for the Landsat sensor and the water surface salinity were selected as independent and dependent variables, respectively. Several techniques exist to estimate the regression equation parameters; we use Least Squares Errors (LSE) in SPSS software. In this method, the line equation coefficients are determined in a manner that has the least square errors (Townend, 2013).

In studies of this nature, the estimated parameter—in this case, surface salinity—is compared with observed data. To this end, key validation metrics, including the root mean square error (RMSE) and correlation coefficient, are employed to assess the results. This approach enables the confirmation of the model's data robustness through the calculation of a 95% confidence interval and sensitivity analysis of input parameters (Tayfehrostami et al., 2021).

Figure 3 shows the Arvand River mouth, satellite image footprint, measuring stations of ROPME oceanographic cruises, and the colored image of the surface salinity derived from ROPME data within the cruises' measurements domain. In regression, the independent variables are usually chosen in ways that have constant distances within their actual variation range (Townend, 2013). Thus, in the ROPME data range (colored image in Figure 4), the points (those marked with a star) were selected to investigate the relationship between the surface salinity and the reflectance values of the Landsat satellite bands, which, in addition to the spatial coverage of the zone, provide the most changes in the reflectance values of the Landsat bands. At star points of Figure 3, the surface salinity and the reflectance values of each satellite band were extracted and then entered into SPSS in tabular form (Table 1). The salinity fluctuations in the selected points are between 36-40 ppt.

In the analysis of satellite imagery for this study, atmospheric correction was conducted using the FLAASH module in ENVI 5, which calculates surface reflectance by compensating for atmospheric effects such as water vapor and dust. Additionally, surface reflectance data corrected by the USGS were obtained, showing minimal differences from the FLAASH results. Consequently, USGS-corrected data were preferred due to their public accessibility. To address the removal of pixels contaminated by clouds, shadows, or land, the Fmask algorithm provided by USGS was applied, which enables the identification of valid water pixels for accurate data extraction.

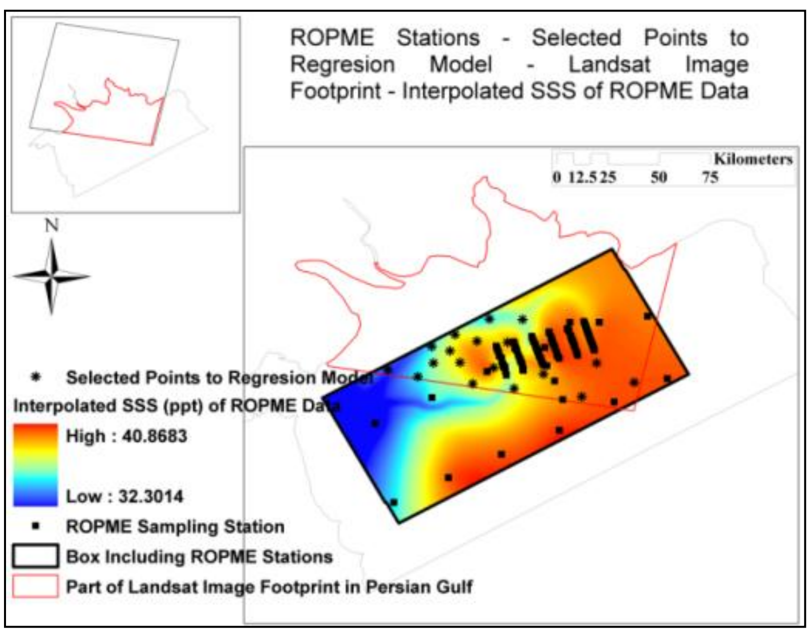

Figure 3. The domain of the Arvand River mouth. The Landsat satellite image footprint (top-left). Squares are the measuring stations of ROPME oceanographic cruises where the seawater parameters, including salinity, were measured. The colored image shows the surface salinity extracted from ROPME data in the measurement domain.

Table 1. Co-located Measured Surface Salinity and Landsat Band Reflectance

NO	LAT	LONG	Salinity	SR_Band1	SR_Band2	SR_Band3	SR_Band4	SR_Band5	SR_Band7
1	29.55	48.496	34.29	1295	1452	972	571	250	243
2	29.519	48.629	36.01	1095	1185	757	571	250	199
3	29.652	48.689	36.10	1095	1185	792	529	221	156
⋮	⋮	⋮	⋮	⋮	⋮	⋮	⋮	⋮	⋮

Note: Coordinates of data points are marked with a star in Figure 2.

In a comprehensive overview, the research methodology is structured around two approaches: remote sensing and numerical modeling. In the modeling component, the relationship between river discharge and plume area has been explored through hydrodynamic simulation utilizing the Finite Volume Community Ocean Model (FVCOM), which encompasses the simulation of hydrodynamic conditions in the Persian Gulf and the evaluation of plume sensitivity to fluctuations in river discharge and diverse wind patterns, implemented through 14 wind scenarios and 8 discharge modes. This process has been finalized with the establishment of a surface salinity threshold of 37 psu as the plume boundary, selected based on its statistical sensitivity to environmental factors. In the remote sensing component, surface salinity at the Arvand River mouth has been derived using Landsat TM-5 imagery, with salinity patterns employed to calculate the plume area. In the subsequent phase, the actual plume area extracted from satellite image processing will be incorporated into the mathematical relationship between river discharge and plume area (PA-RD), thereby yielding a precise estimation of the Arvand River discharge for the year 1992. This flowchart comprehensively outlines the research stages, as depicted in the figure below.

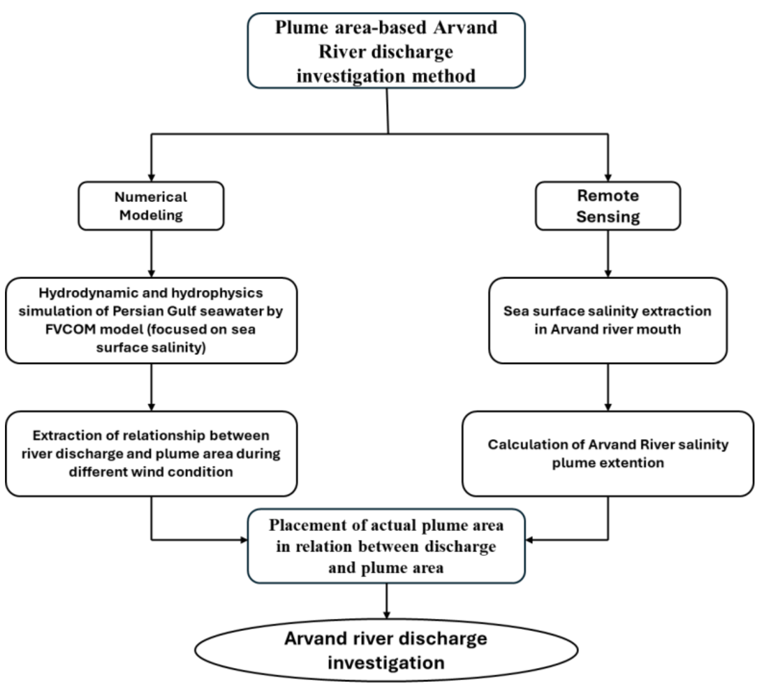

Figure 4. Flowchart of the main research stages. This figure illustrates the primary steps of the study for the indirect estimation of the Arvand River discharge.

3. Results

3.1. Numerical Simulation

As mentioned above, plus the river discharge and wind conditions (controllable parameters), coastal streams (as a background parameter) influence the plume structure. Moreover, since the plume boundary measurement is conducted according to the water surface salinity, along with other parameters, the model should precisely simulate the general water circulation and the surface salinity of the river mouth.

3.1.1. Model Verification and Validation

River discharge and wind conditions are controllable variables in the model (in model experiments, the river discharge and wind are changed) that affect the river plume area. Furthermore, coastal currents -as the background variable- affect the river plume areas. On the other hand, the plume border is determined by sea surface salinity contours. So, the model must correctly simulate salinity, temperature, water circulation, and tide. Tide is one of the variables affecting Persian Gulf circulation. Admiralty tidal data and measurements, current data were collected at several points for model validation and compared with corresponding model data.

In this study, bed friction was used for the model Sensitivity analysis. The simulation was done with various bed frictions. Sensitivity analysis shows that the model has the best tide and current output if bed friction equals 0.03 in depths less than 50 meters and is equal to the model default in depths greater than 50 meters. The left side of Figure 5 compares Admiralty tidal data with the modeled surface water level for different bed friction. The right side of Figure 5 compares measurement data and model data of the current at a point in the center of the north coast of the Persian Gulf (Bushehr).

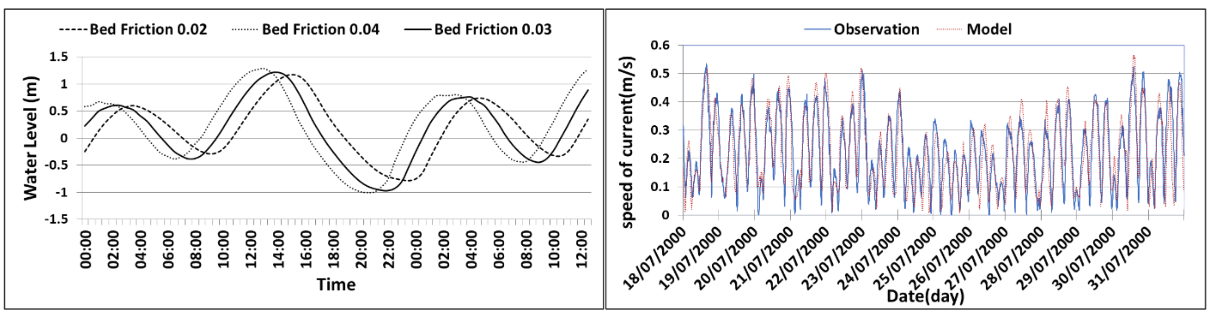

Figure 5. Sensitivity analysis of water level changes near Faw Port based on Admiralty data (left) and current velocity at a station near Bushehr Bay resulting from model implementation and measurement data (right)

Sensitivity analysis for diffusion coefficients revealed that the Smagorinsky model (Smagorinsky, 1963) for Horizontal Diffusion Coefficients and Oceanic Turbulence MY-2.5 model (Mellor & Yamada, 1982) for vertical Diffusion Coefficients are the best choices in the model. The matching of the model results with the temperature and salinity measurement data is due to the correct selection of the model's horizontal and vertical diffusion coefficients. A comparison of the T-S diagrams was obtained from the ROPME measurement data and the model provided in Figure 6.

After the Sensitivity analysis, it is also necessary to ensure the stability and accuracy of the model. Validation of the Model for sea surface temperature and salinity, and tidal results is presented in Figure 7. In this figure, part (a) shows part of the study area and validation and stability checking points, including positions 1 for stability Check, 2 for Sea surface temperature and salinity check, and 3 for tidal check. Part (b) shows the surface salinity of the Arvand River mouth in 500 m3.s1-, without wind and low water slack. According to this figure, it is clear that in March, the surface salinity of the river mouth is equal to 20 ppt, which corresponds to Abdullah's field measurements (Abdullah et al., 2016).

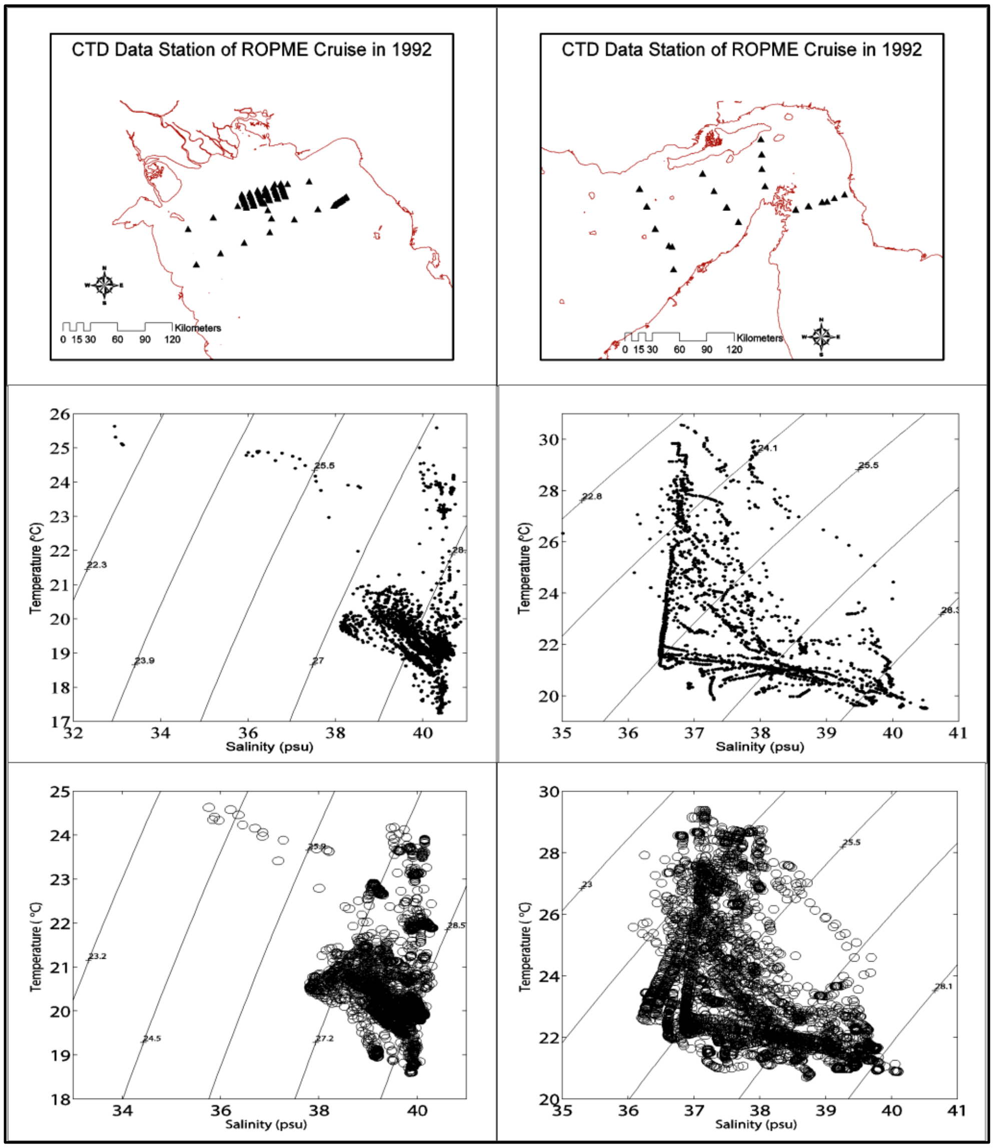

Figure 6. Comparison of temperature-salinity diagrams obtained from the model and data measured during the 1992 ROPME patrol in the northwest Persian Gulf (left) and the Strait of Hormuz (right). (○ Model - ● ROPME)

Figure 7 (c) shows the measurement salinity data at different distances from the mouth of the Arvand River in March, where position 3 is one of the measurement stations (Abdullah et al., 2016). Parts (d and f) show the tides of the model and Admiralty data, respectively, at the mouth of the Arvand River (position 2). Parts (e and g) show the repeatability diagram of temperature and salinity in the last 2 years of the simulation period in position 1, indicating the model's stability. In addition to the visual validations presented in Figures 5, 6, and 7, which demonstrate strong agreement between the model outputs and observations for tidal elevation, sea surface temperature (SST), and sea surface salinity (SSS), a statistical validation was conducted to further quantify model performance. Using data from Admiralty Tide Tables, ROPME 1992 cruise measurements, and field observations by Abdullah et al. (2016), statistical metrics including Root Mean Square Error (RMSE), Mean Absolute Error (MAE), Bias, and Nash-Sutcliffe Efficiency (NSE) were calculated for multiple locations across the modeled domain, including the Arvand River mouth, the Strait of Hormuz, and central Persian

Gulf regions (Figures 5, 6, and 7). Although the model was validated across the entire year to ensure stability, results for March 1992 are emphasized due to their extensive use, supported by the availability of Landsat TM-5 imagery and ROPME data. For tidal elevation, RMSE is 0.022 m, MAE is 0.017 m, Bias is -0.015 m, and NSE is 0.98. For SST, RMSE is 0.122°C, MAE is 0.112°C, Bias is -0.075°C, and NSE is 0.995. For SSS, RMSE is 0.122 psu, MAE is 0.112 psu, Bias is -0.087 psu, and NSE is 0.999. These metrics, consistent with the close alignment observed visually, confirm the model's high accuracy.

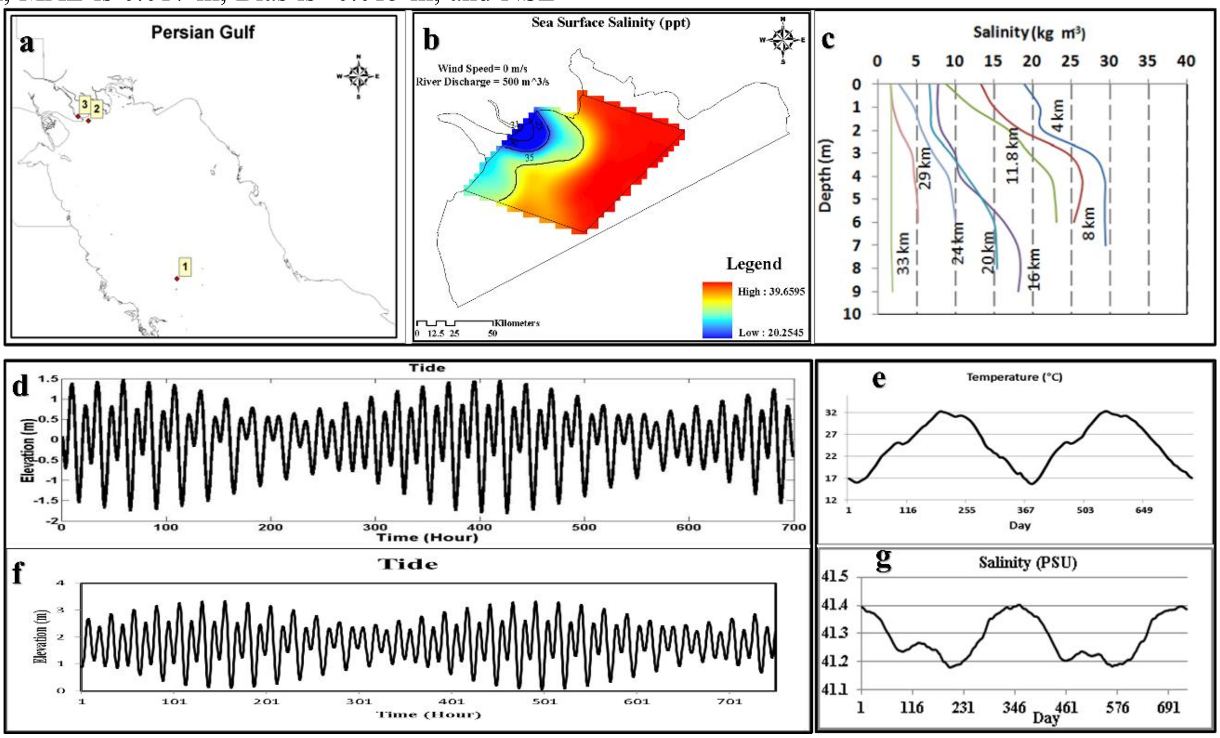

Figure 7. Model validation. a) Part of the model range (Persian Gulf) and the locations of the points for checking the stability of the model (point 1), the verification of tide (point 2), and the closest salinity measurement station in the study (Abdullah et al., 2016) to the river mouth (point 3). B) Surface salinity of the river mouth and the plume formed in the no-wind condition. C) Salinity profile in the Arvand River at different distances from the mouth in March (the bold blue graph belongs to position 3). d) Tide obtained from the model and f) Tide obtained from Admiralty data at position 2. e) Time series of surface temperature and g) surface salinity at position 1 in the last 2 years of the entire simulation period, which indicates the stability of the model.

The counter-clockwise circulation is one of the important features of the Persian Gulf (Kamidis et al., 2015; Reynolds, 1993; Yankovsky & Chapman, 1997) which causes the freshwater of the Arvand River to rotate to the right in no-wind conditions (Kämpf & Sadrinasab, 2006).

Figure 8 shows the surface water circulation of the Persian Gulf obtained from the model. Due to the high-resolution grid of the model, graphical images of arrow currents are not of acceptable quality. For this reason, model outputs of currents were interpolated at fewer points in the Persian Gulf. This figure confirms counter-clockwise circulation in the Persian Gulf and is consistent with previous studies. Also, sea surface temperature and salinity indicate the entry and exit of water from the Persian Gulf and its general circulation.

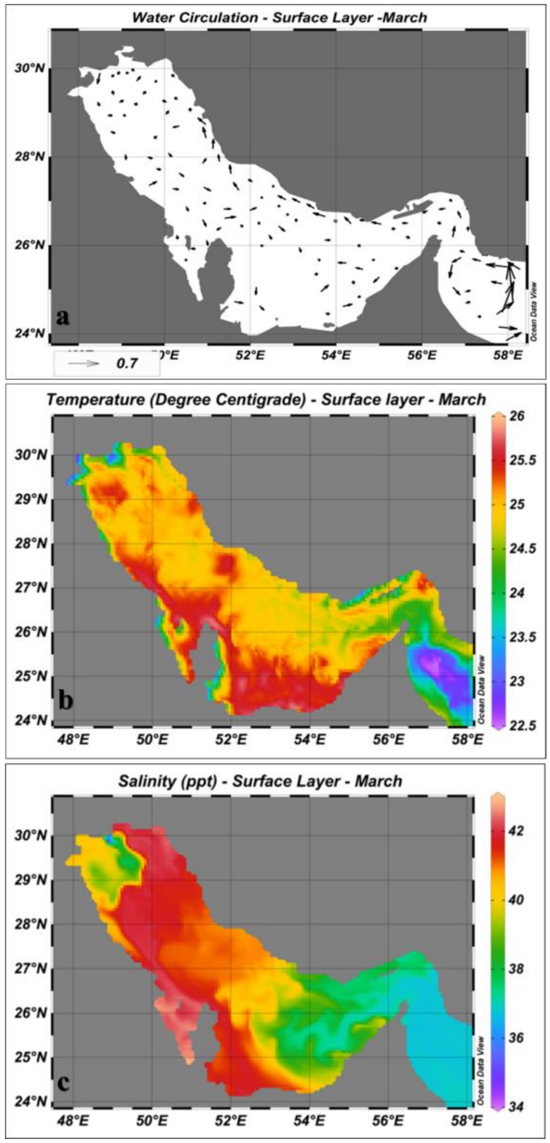

Figure 8. Top: Surface water circulation, Middle: surface temperature, and Bottom: surface salinity of the Persian Gulf in March from model results.

3.1.2. River plume boundary selection

Generally, the surface salinity contour of about 30 psu or 32 psu (which is different for each region) is used as the river plume boundary (Ou et al., 2007; Wang et al., 2008). Statistical data indicate that a salinity of 37 psu, with a standard deviation of 1086.81 and variance of 1181146.54, exhibits greater sensitivity to variations in discharge and wind conditions compared to 33 psu, which has a standard deviation of 349.52 and variance of 122167.44. Furthermore, sensitivity analysis for salinity values between 35 and 39 psu confirms the optimality of 37 psu, as higher values (such as 38 or 39 psu) show reduced variance and lower sensitivity, while 35 psu, with a standard deviation of 745.62 and variance of 555955.63, demonstrates less adaptability to environmental fluctuations. This selection, by yielding a higher coefficient of determination (R^2) in the regression model, enhances the statistical accuracy of the analyses. As a result, the west wind of 2 $m.s^{-1}$ and the northwest wind of 14 $m.s^{-1}$ have the maximum and minimum mean plum areas, respectively.

3.1.3. Plume Type

As already stated, the river plumes are divided into two groups: surface-advected plumes and bottom-advected plumes. In the surface-advected plumes, the shallow buoyant layer overlays denser coastal and continental shelf waters (Yankovsky & Chapman, 1997). The shape and extent of this type of plume can be heavily influenced by wind (Tarya et al., 2015). Although the direction of the wind influences these plumes' extension, their size is determined primarily by the river discharge (Καμίδης et al., 2015). Figure 9 shows a cross-section of the river mouth under the river discharge of 300 $m^3.s^{-1}$ and windless conditions. In the figure, the water stratification is quite clear. The low-salt water is deposited on the surface and completely isolated from the seabed. The salinity cross-section indicates that the river plume (low-salt water) was extended 20 km from the river mouth without interacting with the seafloor. The halocline graph shows water stratification at arbitrary points in the river mouth. As a result, the Arvand River plume is a surface-advected plume type strongly affected by wind conditions. Figure 10 shows the surface salinity of the river mouth under the river discharge of 300 $m^3.s^{-1}$ and different wind conditions. The salinity-temperature diagram is also provided below . These images indicate that the surface water mass displacements in different wind modes only affect the plume shape since the salinity-temperature diagram is very similar in all three modes. These demonstrate that the intense water stratification in the river mouth is the cause of the surface-advected plume creation and illustrate the significant influence of the wind on the plume structure.

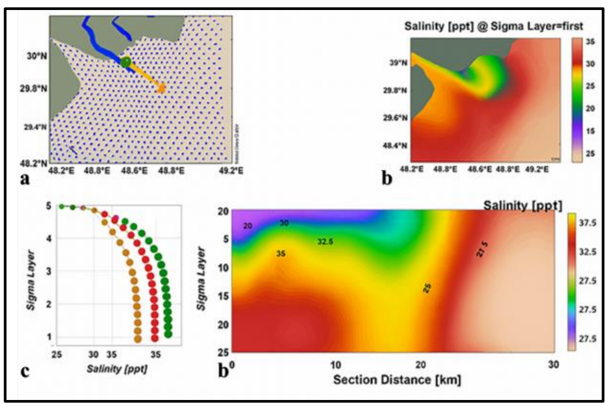

Figure 9. Surface salinity close to the Arvand River mouth for a discharge of 300 $m^3.s^{-1}$ Moreover, no-wind force: a) cross-section location, b) surface salinity, c) salinity profile for some stations near the river mouth, and d) cross-section of salinity.

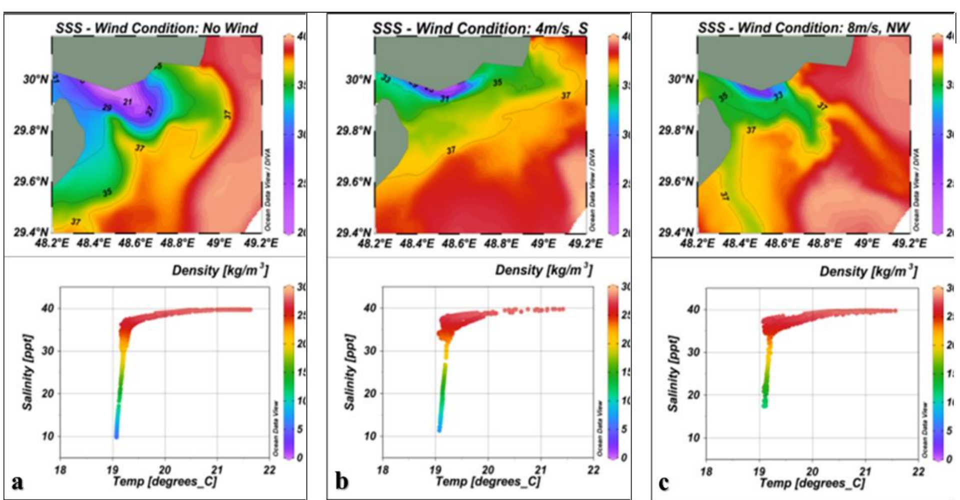

a) no-wind condition	b) south wind of 4 m/s	c) northwest wind of 8 m/s

Figure 10. Surface salinity and corresponding T-S diagram

3.1.4. River discharge and river plume relationship

As the river discharge increases, the area of its plume also expands. Since this is obvious, the following variations of the river discharge area are presented only in one wind mode (4 m/s S). Figure 11 shows the relationship between river plume area and discharge in the no-wind condition. As expected, as the river's discharge increases, its plume area also increases.

By implementing different wind scenarios, three distinct plume patterns emerged, which were categorized into plume categories I, II, and III. Plume Category 1 is diverted toward the north coast, and Plume Category 3 is diverted toward the south coast of the Persian Gulf. Plume Category 2 is almost straight and not diverted to the sides. Plume Category 1 is created by winds from the east-to-south quarter, Plume Category 2 is created by the wind from the west to the east-north sector, and Plume Category 3 is mainly created by north, east, and primarily weak winds. Figure 12 shows these three Categories of plumes.

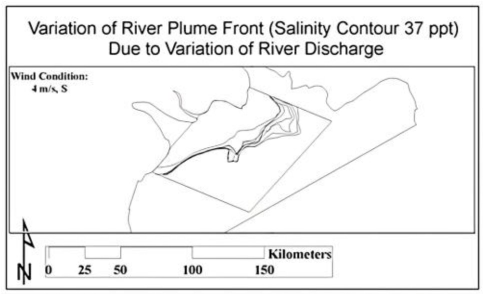

Figure 11. Surface contour of 37 psu as a plume boundary per different river discharges from 300- 650 $m^3.s^{-1}$. Contours representing lower discharges are located near the river mouth, while those corresponding to higher discharges extend further away.

Since wind is the incremental factor of shear stress on the sea surface, an increase in wind speed leads to further mixing in the water column and a decrease in the plume area (Xing & Davies, 1999; Καμίδης et al., 2015). Due to the specific morphology of the coast, different wind conditions have different effects on the river plume area. By north and east winds, the plume deviates toward the south, penetrating the Khor Abdullah south of the river mouth. Increasing shear stress and penetration of the plume to Khor Abdullah reduce the plume area in this situation. Thus, as Figure 13a shows, the plume area decreased significantly as the speed of the north and east winds increased. South and west winds lead to deviation of the river plume toward the north coast. In this case, the plume is expanded due to the water and the collision on the northern coast, compensating for the reduced plume area due to increased shear stress. As Figure 13b shows, as the south and west wind speeds increase, there are no apparent changes in the plume area than the north and east winds. The northwest wind does not cause plume deviations to the sides, and what affects the plume area is the shear stress increased by raising the wind speed, which reduces the plume area (Figure 13c).

Given these dynamics and complications, a single equation cannot very well show the relationship between river discharge and plume area in all of the different wind conditions. Therefore, a unique PA-RD equation is necessary for a more precise estimation of the river plume area from river discharge for each wind condition. So, in this study, considering wind conditions, the intended PA-RD equation was used for river discharge estimation.

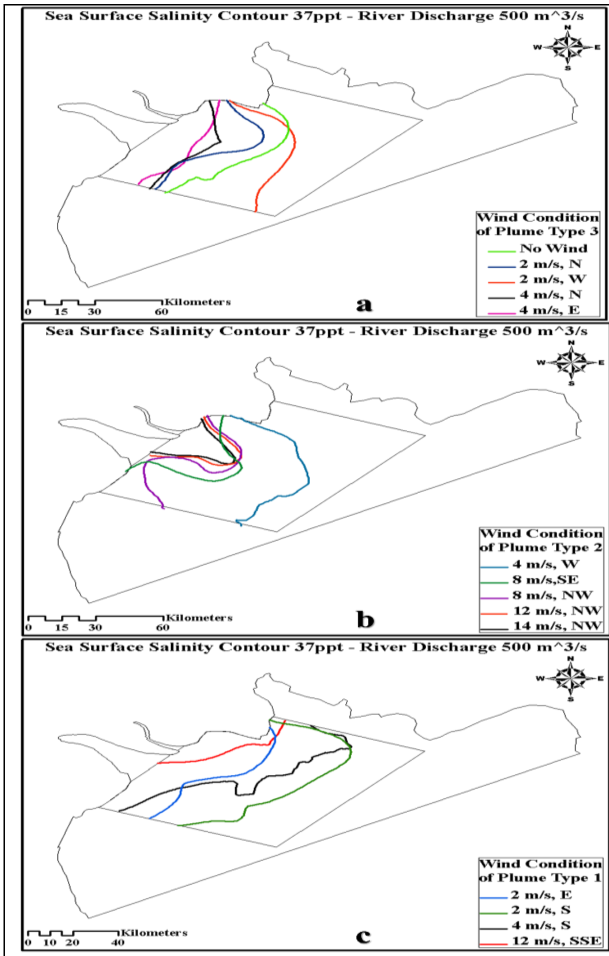

Figure 12. Plume boundary (salinity of 37 psu) at 500 $m^3.s^{-1}$ and different wind modes that cause the creation of the plume Category 1 (a), plume Category 2 (b), and plume Category 3 (c).

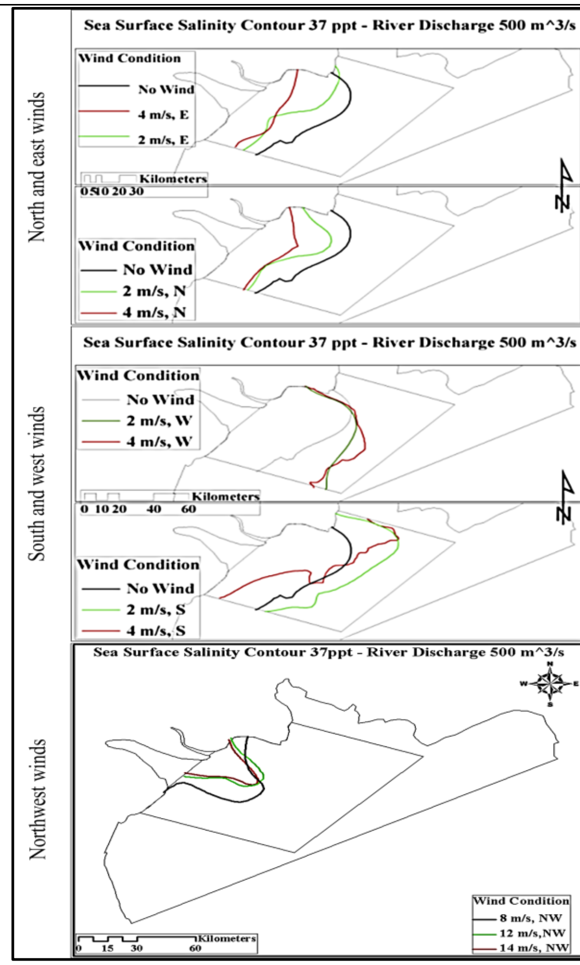

Figure 13. Plume boundary (salinity contour of 37 psu) under a river discharge of 500 $m^3.s^{-1}$ and various wind conditions

In this regard, the PA-RD relationship was calculated for 14 wind conditions as simulations in the numerical model. These 14 wind conditions are the wind conditions of the region based on meteorological data. During each of these simulations, one of the wind conditions was continuously applied to the model. The river discharge reached its maximum value in the model from the minimum value; thus, the PA-RD relationship was calculated for that wind condition. Table 2 shows the PA-RD relationship for different wind conditions of the region (some of the 14 wind conditions are mentioned).

Table 2. PA–RD relationships derived from model simulations under representative wind scenarios

Simulations No	Wind Condition	Regression line	r^2 (coefficient of determination)
1	No wind	*Plume area=2179.19+0.55*River discharge*	0.98
2	2 m/s, N	*Plume area = 1316.93 + 0.672 * River discharge*	0.98
3	2 m/s, W	*Plume area = 2934.365 + 0.712 * River discharge*	0.97
4	4 m/s, W	*Plume area = 1229.11 + 3.838 * River discharge*	0.94
5	12 m/s, SSE	*Plume area = 282.03 + 0.379 * River discharge*	0.94
⋮	⋮	⋮	⋮

Note: A selection of wind scenarios, drawn from the 14 applied cases, is presented for reference.

3.2. Remote sensing

The scatter plot represents the linear relationship between the surface salinity and reflectance for Landsat image bands 2 and 3 (Figure 14). The multivariable regression model, using the stepwise method, indicated that only Landsat bands 2 and 3 are suitable for extracting the regression equation. The coefficient of determination of the regression model is 0.87. It was found through the analysis of variance (ANOVA) table that the regression model with an index F of 49.93 and a P-value close to zero is good. The intercept coefficient and the bands 2 and 3 coefficients were determined at 48.62, -0.004, and -0.009; the P-value for each was approximately zero. Therefore, the surface salinity was extracted using the reflectance for the Landsat bands 2 and 3 according to the SSS-SR relation within the ROPME oceanographic cruises data. The SSS-SR relation was obtained as

$SSS = 48.628 - 0.004(SR_{Band2}) - 0.009(SR_{Band3})$.

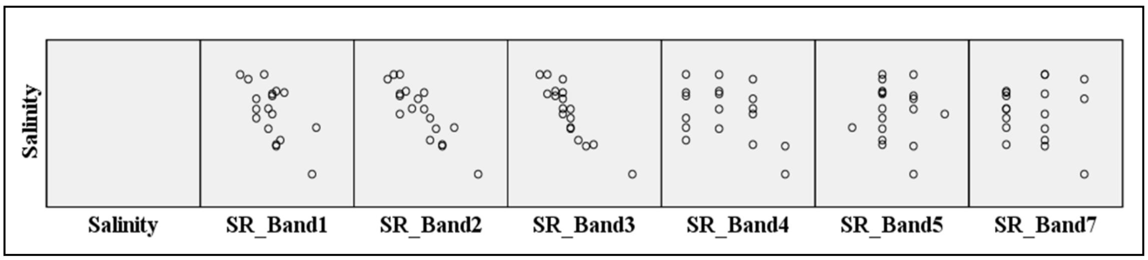

Figure 14. Distribution diagram between the surface salinity and the surface reflectance for different Landsat bands.

Figure 15 shows the normal probability plot of the regression standardized residual dependent variable and the scatter plot of standardized residuals (ZRESID) versus standardized predicted values (ZPRED). These plots represent the randomness and the constant of the residual variance, which are the requirements of the regression model.

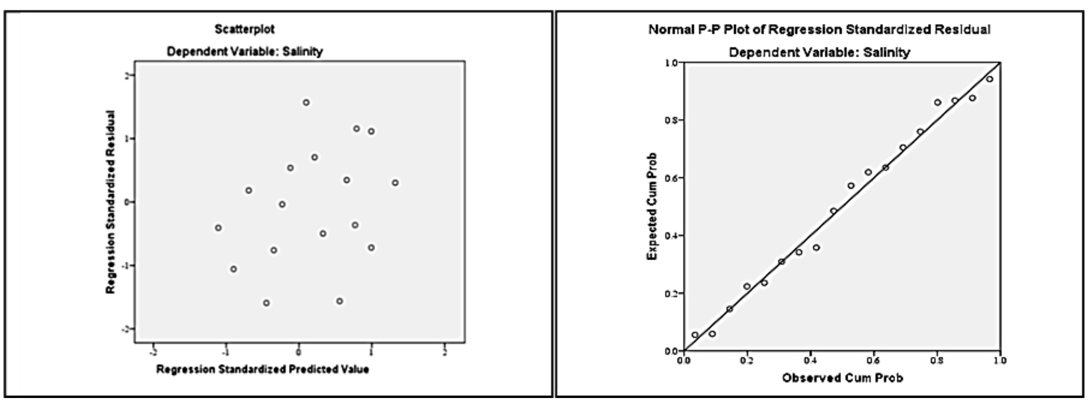

Figure 15. a) Normal P-P plot of the regression standardized residual dependent variable. b) Scatter plot of standardized residuals (ZRESID) versus Standardized predicted values (ZPRED).

To further validate the model, the estimated surface salinity was compared with in situ data from reference stations. The surface salinity, derived from the equation SSS = 48.628 - 0.004 * SR_Band2 - 0.009 * SR_Band3, exhibited a root mean square error (RMSE) of 0.561 psu and a 95% confidence interval for the mean estimated salinity of [36.78, 37.52] psu. These findings demonstrate the model's accuracy in estimating surface salinity at the Arvand River mouth.

Figure 16 illustrates the surface salinity obtained by applying the SSS-SR relation over Landsat bands 2 and 3. It is evident that salinity increases as the distance from the river mouth increases, and the pattern exhibited is in accordance with the statute of the surface salinity in the zone. Therefore, we can only rely on the surface salinity extracted from satellite imagery, which is between 36-40 psu.

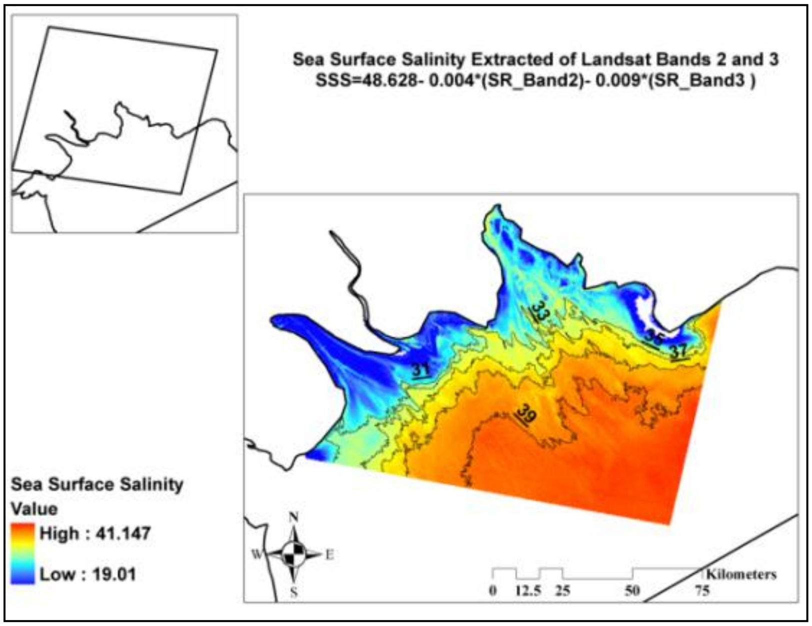

Figure 16. Salinity extracted from the Landsat satellite TM5 images on March 5, 1992.

4. Discussion

We found that in the river mouth, the water column has been significantly stratified, and the river freshwater deposited on the seawater causes the formation of the surface-advected plume. In no-wind conditions, the river plume is affected by the general water circulation of the Persian Gulf, and the Coriolis effect deviates toward the south coast of the Persian Gulf. The Arvand River plume exhibits significant sensitivity to wind conditions, with its spatial extent generally diminishing as wind speed intensifies, a pattern consistent with the findings of Collins and Macdonald (2025), who demonstrated that wind forcing substantially influences plume variability in Hawke's Bay. The Arvand River mouth's coastal morphology also impacts the river plume's structure. North winds further deviate the plume toward the south and penetrate Khor Abdullah, which, combined with the wind's shear stress factor, reduces the plume area. The river plume is generally categorized into three modes under different wind conditions. Although the plume shape is entirely different in various wind modes, the difference is only due to the displacement of the surface water mass, as the similarity of temperature-salinity diagrams in different modes can prove.

It is emphasized that, in addition to the river discharge, the river plume area is also strongly affected by wind conditions and, to some extent, by the Persian Gulf water circulation. Therefore, it is impossible to extract a suitable and strong relationship that determines the relationship between the river discharge and the plume area (PA-RD). Therefore, the PA-RD relationship was extracted under different regional wind conditions. In other words, for 14 wind conditions in the region that were applied in the model, 14 PA-RD relationships were also obtained. For this reason, the wind conditions should first be determined to extract the plume area, and then the PA-RD should be used.

Accordingly, the wind data was collected from the ECMWF data about 6 hours before the satellite recorded the image. In this case, the wind field at the mouth of the river was from the south and had a speed of about 3 $m.s^{-1}$ (Figure 17). This plume structure and its area were simulated by implementing this wind (3 $m.s^{-1}$) in the model. The results demonstrate that the south winds cause the plume category 1 creation, which extends toward the northern coasts. Then, the sensitivity of the plume area to the river discharge was examined under the south winds of 3 $m.s^{-1}$ using the numerical simulations (Figure 18, Left). According to the data and with the regression model, the PA-RD relation was obtained in the wind mode of 3 $m.s^{-1}$ as follows;

$$Plume\ area = 1533 + 2.71 \times River\ discharge.$$

Then, the river plume area with a boundary as a salinity contour of 37 psu was extracted from the satellite images. This plume area was calculated to be 2996 km^2 (Figure 18, Right).

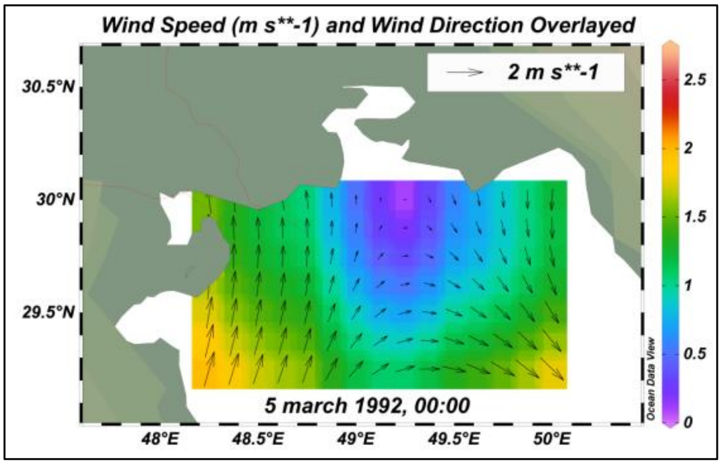

Figure 17. Wind field in the Arvand River mouth at about 6 hours before the satellite recorded the image

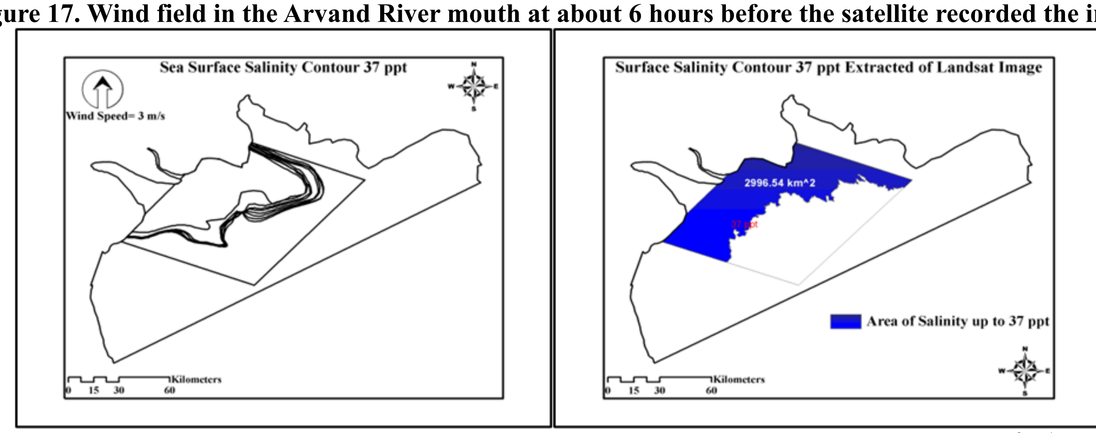

Figure 18. Left: Enhancement of Plume area by river discharge enhancement from 350-650 m^3.s^{-1} under the wind of 3 m s-1. Right: Plume area with a salinity of 37 psu that was extracted from the Landsat imagery

According to the PA-RD and considering the plume area of 2996 km^2 that was extracted from the Landsat images, the river discharge was estimated to be 540 m^3.s^{-1} in March 1992. The maximum discharge of the Arvand River is between March and May (Flint et al., 2011). Based on the meteorological data, 1992 saw high rainfall within the Arvand River basin. Given the facts, the estimate conducted for the river discharge seems logical.

To complement the analyses of the PA-RD relation under south wind conditions with a speed of 3 m/s (Figures 17 and 18), the 95% confidence interval for the relationship PA = 1533 + 2.71 * RD was calculated. Using this relationship and the estimated discharge of 540 m³/s, the predicted plume area is 2996.4 km² with a 95% confidence interval of [2957, 3036] km², which closely aligns with the satellite-derived plume area of 2996 km² from Landsat TM-5 imagery. These results confirm that the estimated discharge of 540 m³/s, derived by comparing the satellite-derived plume area with the PA-RD relationship, is consistent with the maximum discharge period of the Arvand River in March 1992 (Flint et al., 2011) and the high rainfall recorded in that year.

Furthermore, statistical analyses, including a Monte Carlo simulation assuming a uniform discharge distribution (300–650 m³/s) and a ±5% error in the satellite-derived plume area, yielded an uncertainty range for the estimated discharge of 540 m³/s within [485, 595] m³/s. This uncertainty range is reasonable given the seasonal variability of the river discharge and the influence of south winds on the plume structure.

The results obtained from applying the indirect method to measure the discharge of the Arvand River, which has not been directly measured to date, carry significant implications for transboundary water management, climate change impacts, and the ecological health of the Persian Gulf. From a water management perspective, accurate discharge estimation can serve as a foundation for negotiations among the riparian countries of the region regarding the equitable allocation of Arvand water resources, particularly given the political challenges that restrict access to in-situ data. Furthermore, variations in the Arvand's discharge may reflect the effects of climate change, such as reduced rainfall or increased evaporation in the Persian Gulf region, influencing the hydrologic cycle. Additionally, the influx of freshwater from the Arvand into the Persian Gulf moderates surface salinity, impacting sensitive ecosystems, including coral reefs and aquatic species, thus underscoring the need for continuous monitoring. The findings of this study align with limited similar research conducted in the region, including the study by Tayfehrostami et al. (2021), which monitored the Karun River discharge using Sentinel data, reinforcing the necessity of advancing remote sensing techniques for sustainable water resource management in the region.

5. Conclusion

This study is one of the most severe works that has ever been done to get a good understanding of the Arvand River discharge. Given the severe climate changes in the region and the unstable conditions, which make it impossible to directly and accurately measure this river's discharge, it is essential and highly recommended to continue such research to clarify this important river's discharge in the region. Although the river discharge was not directly measured using this method, it provided a reasonable estimate of the river discharge. Therefore, using this method in this region, where there is no standard information on river discharge, is very important. This method can also be used to examine changes in river discharge since satellite images and suitable ground data are available.

Although this study, through the innovative application of diverse methodologies, successfully addressed the challenge of limited discharge data for the Arvand River in a region characterized by severe environmental data scarcity, providing valuable estimates, it is not without limitations. The reliance on a single, limited, reliable dataset (the 1992 ROPME cruise) constrains the model's generalizability, while the absence of direct discharge measurements introduces uncertainty in linking salinity to river discharge. To mitigate these limitations, it is recommended that the dataset be expanded through international collaboration, incorporating regular in-situ discharge measurements, and that the integration of multi-sensor satellite data alongside advanced hydrodynamic models be pursued to enhance the accuracy of estimations, thereby supporting the sustainable management of this critical water system.

Acknowledgment

This research was conducted as part of a Ph.D. dissertation at KMSU and was generously supported by the Iranian Port and Maritime Organization (PMO). The authors are sincerely grateful to RM Reynolds for providing access to the ROPME dataset. We extend our heartfelt thanks to all individuals and institutions whose contributions and support made this work possible.

Author Contributions:

Abbas Einali: Led the numerical modeling process, performed statistical analyses, and applied remote sensing and GIS techniques. He was also responsible for interpreting the results and drafting the manuscript.

Masoud Sadrinasab: Contributed to the interpretation of the numerical modeling results and provided analytical insights during the evaluation phase.

Mohammad Akbarinasab: Assisted in the implementation of remote sensing and GIS methods and supported the interpretation of geospatial data.

Jafar Azizpour: Collaborated in the setup and execution of the numerical model, contributing to its technical development and operational deployment.

Conflicts of interest

The authors of this article declared no conflict of interest regarding the authorship or publication of this article.

Data availability statement:

All data generated or analyzed during this study are included in this published article.

References

Abdullah, A. D., Gisen, J. I., Zaag, P. v. d., Savenije, H. H., Karim, U. F., Masih, I., & Popescu, I. (2016). Predicting the salt water intrusion in the Shatt al-Arab estuary using an analytical approach. Hydrology and earth system sciences, 20(10), 4031-4042. doi: 10.5194/hess-20-4031-2016

Al-Aesawi, Q., Al-Nasrawi, A. K., Jones, B. G., & Yang, S.-Q. (2021). Geomatic freshwater discharge estimations and their effect on saltwater intrusion in alluvial systems: a case study in Shatt Al-Arab estuary. Environmental Earth Sciences, 80, 1-15. doi: 10.1007/s12665-021-09945-4

Bricker, J. D., Okabe, I., & Nakayama, A. (2006). Behavior of a small pulsed river plume in a strong tidal cross-flow in the Akashi Strait. Environmental Fluid Mechanics, 6(3), 203-225. doi: 10.1007/s10652-006-9013-4

Chao, S.-Y. (1988). River-forced estuarine plumes. Journal of Physical oceanography, 18(1), 72-88. doi: 10.1175/1520-0485(1988)018<0072:RFEP>2.0.CO;2

Chao, S.-Y., & Boicourt, W. C. (1986). Onset of estuarine plumes. Journal of Physical oceanography, 16(12), 2137-2149. doi: 10.1175/1520-0485(1986)016<2137:OOEP>2.0.CO;2

Chen, C., Beardsley, R. C., & Cowles, G. (2006). An unstructured grid, finite-volume coastal ocean model: FVCOM user manual. SMAST/UMASSD. doi: 10.5670/oceanog.2006.92

Cheng, R. (2000). Defining hydrologic instrumentation for the 21st Century. search of techniques for monitoring river discharge. US Geol. Survey Remote-Sensing Workshop (Menlo Park, California, USA,

Collins, C., & Macdonald, H. S. (2025). Modelling the variability and dynamics of river plumes in Hawke’s Bay, Aotearoa New Zealand. Frontiers in Marine Science, 12, 1536550. doi: 10.3389/fmars.2025.1536550

Duenwald, M. C., Abdih, M. Y., Gerling, M. K., Stepanyan, V., Al-Hassan, A., Anderson, G., Baum, M. A., Saksonovs, M. S., Agoumi, L., & Chen, C. (2022). Feeling the Heat: Adapting to Climate Change in the Middle East and Central Asia. International Monetary Fund. doi: 10.5089/9781513591094.087

Duvvuri, B., Gehring, J., & Beighley, E. (2024). Methodological evaluation of river discharges derived from remote sensing and land surface models. Scientific Reports, 14(1), 25653. doi: 10.1038/s41598-024-75361-w

Eddin, M. H. S., Zahng, Y., Kollet, S., & Gall, J. (2025). RiverMamba: A State Space Model for Global River Discharge and Flood Forecasting. arXiv preprint arXiv:2505.22535. doi: 10.48550/arXiv.2505.22535

Flint, A., Flint, L., Curtis, J., & Boesch, C. (2011). A Preliminary Water Balance Model for the Tigris and Euphrates River System. In: USGS.

Garvine, R. W. (1981). Frontal jump conditions for models of shallow, buoyant surface layer hydrodynamics. Tellus, 33(3), 301-312. doi: 10.3402/tellusa.v33i3.10717

Garvine, R. W. (1982). A steady state model for buoyant surface plume hydrodynamics in coastal waters. Tellus, 34(3), 293-306. doi: 10.3402/tellusa.v34i3.10813

Garvine, R. W. (1995). A dynamical system for classifying buoyant coastal discharges. Continental Shelf Research, 15(13), 1585-1596. doi: 10.1016/0278-4343(94)00065-U

Global Runoff Data Centre (GRDC). World Meteorological Organization WMO and Federal Institute of Hydrology (BfG). https://grdc.bafg.de/data/data_portal/

Gonçalves, H., Teodoro, A. C., & Almeida, H. (2012). Identification, Characterization and Analysis of the Douro River Plume From MERIS Data. IEEE Journal of Selected Topics in Applied Earth Observations and

Remote Sensing, 5(5). doi: 10.1109/JSTARS.2012.2199740

Jafar, A., Vahid, C., Maziar, K., & Abbas, E. (2014). Study of the Physical Oceanographic Properties of the Persian Gulf, Strait of Hormuz and Gulf of Oman Based on PG-GOOS CTD Measurements. Journal of the Persian Gulf, 5(18), 12. https://www.researchgate.net/profile/Jafar-Azizpour/publication/285581886_Study_of_the_Physical_Oceanographic_Properties_of_the_Persian_Gulf_Strait_of_Hormuz_and_Gulf_of_Oman_Based_on_PG-GOOS_CTD_Measurements/links/568121d208ae1975838f62af/Study-of-the-Physical-Oceanographic-Properties-of-the-Persian-Gulf-Strait-of-Hormuz-and-Gulf-of-Oman-Based-on-PG-GOOS-CTD-Measurements.pdf. [In Persian]

Kamidis, Sylaios, & Tsihrintzis. (2015). Nestos River plume dynamics under variable physical forcing. Πανελλήνια και Διεθνή Γεωγραφικά Συνέδρια, Συλλογή Πρακτικών, 549-566. http://geolib.geo.auth.gr/index.php/pgc/article/view/10460/10208

Kämpf, J., & Sadrinasab, M. (2006). The circulation of the Persian Gulf: a numerical study. Ocean Science, 2(1), 27-41. doi: 10.5194/os-2-27-2006

Karami, N. (2019). The modality of climate change in the Middle East: drought or drying up? J Interrupted Stud 2 (1): 118–140. In.

Khorram, S. (1982). Remote sensing of salinity in the San Francisco Bay Delta. Remote Sensing of Environment, 12(1), 15-22. doi: 10.1016/0034-4257(82)90004-9

Klein, L., & Swift, C. (1977). An improved model for the dielectric constant of sea water at microwave frequencies. IEEE Journal of Oceanic Engineering, 2(1), 104-111. doi: 10.1109/JOE.1977.1145319

Koblinsky, C., Hildebrand, P., LeVine, D., Pellerano, F., Chao, Y., Wilson, W., Yueh, S., & Lagerloef, G. (2003). Sea surface salinity from space: Science goals and measurement approach. Radio Science, 38(4). doi: 10.1029/2001RS002584

KOMIJANE, F., NASROLLAHEE, A., NAHEID, S., & NAZARI, N. (2014). The Persian Gulf wind analysis using meteorological synoptic stations data. NIVAR Journal of Meteorological Organization, 38, 27-44. https://nivar.irimo.ir/article_13157_84e92d58f9b03ffe469397bb3e6fd9a6.pdf?lang=en. [In Persian]

Kourafalou, V. H., Oey, L. Y., Wang, J. D., & Lee, T. N. (1996). The fate of river discharge on the continental shelf: 1. Modeling the river plume and the inner shelf coastal current. Journal of Geophysical Research: Oceans, 101(C2), 3415-3434. doi: 10.1029/95JC03024

Lagerloef, G. S., Swift, C. T., & Le Vine, D. M. (1995). Sea surface salinity: The next remote sensing challenge. Oceanography, 8(2), 44-50. doi: 10.5670/oceanog.1995.17

Legleiter, C. J., Grant, G., Bae, I., Fasth, B., Yager, E., White, D. C., Hempel, L., Harlan, M. E., Leonard, C., & Dudley, R. (2025). Remote sensing of river discharge based on critical flow theory. Geophysical Research Letters, 52(9), e2025GL114851. doi: 10.1029/2025GL114851

Liu, J. T., Chao, S.-Y., & Hsu, R. T. (1999). The influence of suspended sediments on the plume of a small mountainous river. Journal of Coastal Research, 1002-1010. https://www.jstor.org/stable/4299020

Ma, C., He, W., Zhang, G., Li, X., & Zhao, J. (2025). Spatiotemporal variations in Pearl River plume dispersion over the last decade based on VIIRS-derived sea surface salinity. Marine Pollution Bulletin, 218, 118179. doi: 10.1016/j.marpolbul.2025.118179

Mellor, G. L., & Yamada, T. (1982). Development of a turbulence closure model for geophysical fluid problems. Reviews of Geophysics, 20(4), 851-875. doi: 10.1029/RG020i004p00851

Miller, J. L., Goodberlet, M. A., & Zaitzeff, J. B. (1998). Airborne salinity mapper makes debut in coastal zone. Eos, Transactions American Geophysical Union, 79(14), 173-177. doi: 10.1029/98EO00126

Osadchiev, A. (2015). A method for quantifying freshwater discharge rates from satellite observations and Lagrangian numerical modeling of river plumes. Environ. Res. Lett, 10. doi: 10.1088/1748-9326/10/8/085009

Ou, S., Zhang, H., Wang, D., & He, J. (2007). Horizontal characteristics of buoyant plume off the Pearl River Estuary during summer. Journal of Coastal Research, SI, 50, 652-657. https://www.jstor.org/stable/26481667

Reynolds, R. M. (1993). Physical oceanography of the Gulf, Strait of Hormuz, and the Gulf of Oman—Results from the Mt Mitchell expedition. Marine Pollution Bulletin, 27, 35-59. doi: 10.1016/0025-326X(93)90007-7

Robert Brakenridge, G., Cohen, S., Kettner, A. J., De Groeve, T., Nghiem, S. V., Syvitski, J. P. M., & Fekete, B. M. (2012). Calibration of satellite measurements of river discharge using a global hydrology model. Journal of Hydrology, 475, 123-136. doi: 10.1016/j.jhydrol.2012.09.035

Selch, D. (2012). Comparing salinity models in Whitewater Bay using remote sensing. FLORIDA ATLANTIC UNIVERSITY. https://search.proquest.com/openview/39474e9cd0d7ebba0cb8ee600e3427cf/1?pq-origsite=gscholar&cbl=18750

Smagorinsky, J. (1963). General circulation experiments with the primitive equations: I. The basic experiment. Monthly weather review, 91(3), 99-164. doi: 10.1175/1520-0493(1963)091<0099:GCEWTP>2.3.CO;2

Swift, C. T., & Mcintosh, R. E. (1983). Considerations for microwave remote sensing of ocean-surface salinity. IEEE Transactions on Geoscience and Remote Sensing(4), 480-491. doi: 10.1109/TGRS.1983.350511

Tarya, A., Van der Vegt, M., & Hoitink, A. (2015). Wind forcing controls on river plume spreading on a tropical continental shelf. Journal of Geophysical Research: Oceans, 120(1), 16-35. doi: 10.1002/2014JC010456

Tayfehrostami, A., Ardalan, A. A., & Pourmina, A. H. (2021). River discharge monitoring using satellite missions: Sentinel-1, Sentinel-2, and Sentinel-3 (Case study: The Karun River, Iran). Earth Observation and Geomatics Engineering, 5(2), 96-111. doi: 10.22059/eoge.2022.336941.1112. [In Persian]

Townend, J. (2013). Practical statistics for environmental and biological scientists. John Wiley & Sons. https://www.wiley.com/en-us/Practical+Statistics+for+Environmental+and+Biological+Scientists-p-9780471496656

UN-ESCWA, B. (2013). United Nations economic and social commission for western Asia; Bundesanstalt für Geowissenschaften und Rohstoffe. Inventory of Shared Water Resources in Western Asia, Beirut. https://www.unescwa.org/sites/default/files/pubs/pdf/e_escwa_sdpd_13_inventory_e.pdf

Urquhart, E. A., Zaitchik, B. F., Hoffman, M. J., Guikema, S. D., & Geiger, E. F. (2012). Remotely sensed estimates of surface salinity in the Chesapeake Bay: A statistical approach. Remote Sensing of Environment, 123, 522-531. doi: 10.1016/j.rse.2012.04.008

Wang, Q., Guo, X., & Takeoka, H. (2008). Seasonal variations of the Yellow River plume in the Bohai Sea: A model study. Journal of Geophysical Research, 113(C8). doi: 10.1029/2007jc004555

Wiseman, W., & Garvine, R. (1995). Plumes and coastal currents near large river mouths. Estuaries, 18(3), 509-517. doi: 10.2307/1352368

Xing, J., & Davies, A. M. (1999). The effect of wind direction and mixing upon the spreading of a buoyant plume in a non-tidal regime. Continental Shelf Research, 19(11), 1437-1483. doi: 10.1016/S0278-4343(99)00025-4

Yankovsky, A. E., & Chapman, D. C. (1997). A simple theory for the fate of buoyant coastal discharges. Journal of Physical oceanography, 27(7), 1386-1401. doi: 10.1175/1520-0485(1997)027<1386:ASTFTF>2.0.CO;2.